Combining Progressive Nodal Release with the Virtual Crack Closure Technique to Model Fatigue Delamination Growth Without Re-meshing

N.V. De Carvalho[1], R. Krueger[2]
National Institute of Aerospace, Hampton, VA 23666

G.E. Mabson[3], L.R. Deobald[4]
The Boeing Company, Seattle, WA, 98124

Abstract

The present work summarizes an approach to model mixed-mode 3D fatigue crack growth using the Virtual Crack Closure Technique (VCCT) without requiring re-meshing. It is demonstrated that the proposed approach can be used to simulate crack shapes that do not conform to the underlying mesh. The proposed approach relies solely on Paris Law characterization data to model delamination growth. Growth is determined as a post-processing step at the end of each increment, and hence no convergence issues associated with the progressive nodal release are encountered. This approach can be readily applied using standard solid element formulations and is implemented via an interface user element in Abaqus/Standard.

I. Introduction

Delamination is one of the most common and critical failure modes in composites. Within the Finite Element Method framework, Virtual Crack Closure Technique (VCCT) (e.g., [1-4]) and Cohesive Zone (CZ) approaches (e.g., [5, 6]) have become the most accepted techniques for simulating delamination propagation in composites, and have reached sufficient maturity to be available in several commercial simulation software packages. Modeling crack growth in an automated fashion, based on the energy release rates computed using VCCT, requires a separate strategy. One such strategy consists in, at each growth increment, updating the mesh near the crack front such that it conforms to the crack shape as it evolves. This method typically renders very accurate results [7, 8]. However, in fatigue, the main challenges in using this method arise from the difficulties in updating the mesh in cases involving multiple delaminations developing at the same interface or the modeling of overlapping delaminations at immediately adjacent interfaces.

Another strategy can be found in literature [9-11] in which delamination is propagated without updating the mesh by releasing penalty stiffnesses associated with each element or node. However, as a result of this procedure, the shape of the crack front is forced to conform to the underlying mesh, leading to the development of artificial local stress concentrations which affect the accuracy of the energy release rate calculations. Recognizing this limitation, particularly for cracks that develop with an arbitrary shape, several methods have been proposed to alleviate the artificial local stress concentrations and their effect on the energy release rate calculation. These methods typically focus on the use of correction factors applied to the energy release rate VCCT expression [9-11]. These correction factors are not always trivial to determine and implement, particularly for multiple interacting delaminations, and do not eliminate the effect of the artificial stress concentrations completely.

An alternative approach [12] was proposed in which intermediate crack positions, that do not conform to the mesh, are accommodated by allowing the nodes to be released progressively. The approach was implemented via an interface element [12, 13] and applied to the simulation of delamination growth in 2D. A similar approach has been implemented in Abaqus/Standard [14] and can be applied to simulate delamination growth in 3D, but is presently limited to quasi-static applications.

The present work gives rigor to the synchronized mixed mode nodal release based on fracture mechanics principles, extending and formalizing the methodology proposed in [12] to enable modelling of mixed-mode fatigue delamination growth in 3D.

---

[1] Senior Research Engineer, National Institute of Aerospace.
[2] Associate Research Fellow, National Institute of Aerospace.
[3] Technical Fellow, The Boeing Company.
[4] Technical Fellow, The Boeing Company.

II. Formulation

In the present section, details of the proposed formulation are provided, including the procedures used to determine the energy release rates, the crack growth increment, and the progressive nodal release. In addition, details on an optional smoothing algorithm and on the overall implementation are provided.

A. Virtual Crack Closure Technique

For each node i at the crack front, see Fig. 1, the energy release rates are calculated using the classic VCCT expressions:

$$\begin{aligned} G_I^{i,j} &= \frac{1}{2A^i} F_z^i \delta_z^j \\ G_{II}^{i,j} &= \frac{1}{2A^i} F_x^i \delta_x^j \\ G_{III}^{i,j} &= \frac{1}{2A^i} F_y^i \delta_y^j \end{aligned} \tag{1}$$

where F_k^i designates the forces obtained at node i along the directions $k = \{x, y, z\}$ and δ_k^j is the displacement jump computed at an adjacent node j:

$$\delta_k^j = u_k^{j^+} - u_k^{j^-} \tag{2}$$

where $u_k^{j^+}$ and $u_k^{j^-}$ are the displacement computed at the top and bottom surface of the interface at the nodal position j. The area A^i is defined by:

$$A^i = a_l^i a_w^i \tag{3}$$

where a_l^i and a_w^i are defined as illustrated in Fig. 1. The total energy release rate can be obtained by:

$$G_T^{i,j} = G_I^{i,j} + G_{II}^{i,j} + G_{III}^{i,j} \tag{4}$$

The energy release rate determination is automated by calculating Eq. (4) for all adjacent node pairs j that have been completely released. Finally, the maximum energy release rate associated with node pair i is obtained by determining the maximum of the energy release rates computed using the displacement jump determined at each of the four immediately adjacent nodes, j to $j + 3$:

$$G_{T_{max}}^i = max\{G_T^{i,j}, \dots, G_T^{i,j+3}\} \tag{5}$$

In the case illustrated in Fig. 1, only node j will have a nonzero displacement jump since nodes $j + 1$, $j + 2$ and $j + 3$ are not at the crack wake, therefore $G_{T_{max}}^i = G_T^{i,j}$. Note however, that in a general case, the displacement jumps at nodes $j + 1$, $j + 2$ and $j + 3$ may not be zero.

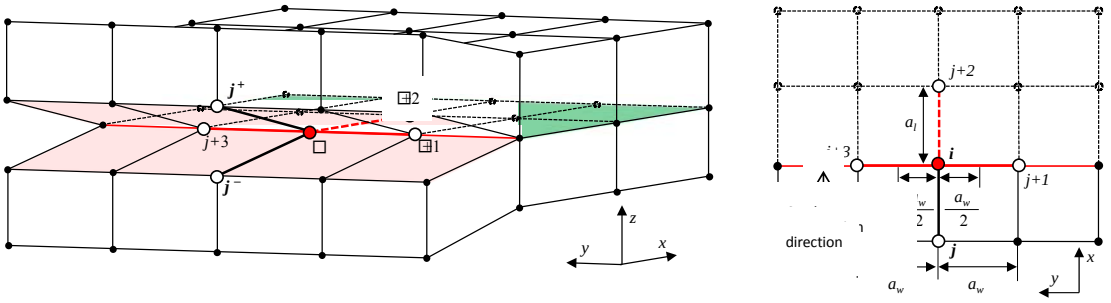

(a) 3D view (deformed) (b) Planar view (un-deformed)

Fig. 1 Crack front illustration and nomenclature.

B. Progressive Release

Based on a given material model, assume the crack grows past the node position i to some intermediate position. In order to represent that propagation, a kinematic constraint is inserted between the top and bottom surface nodes at the nodal position i, which can be thought of as springs connecting their degrees of freedom. The stiffness of these springs is decreased as required, progressively releasing the top and bottom surface nodes at the nodal position i. This procedure is illustrated in Fig. 2~~Fig. 2~~. Here, the progressive nodal release is intended to represent intermediate crack positions between node pairs, and it is not a material constitutive response as in cohesive element formulations. This progressive release procedure results in a region across the crack front, where nodes may be at an intermediate stage of release, held by springs with different stiffnesses. While this region is akin to a process zone obtained in cohesive element formulations, the length of this process zone will not exceed the distance between node pairs.

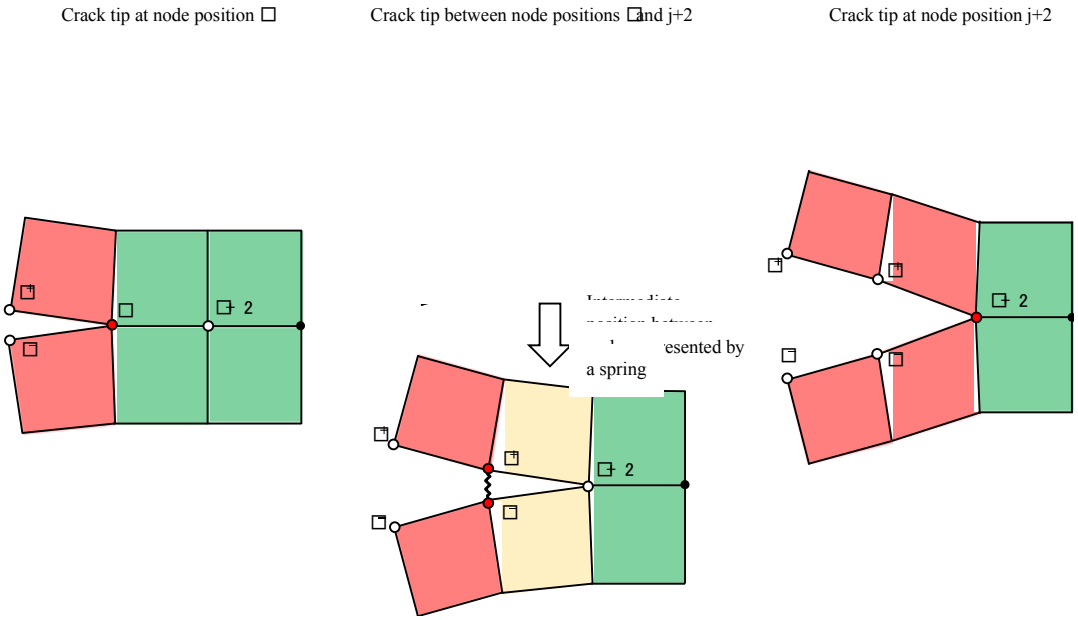

Fig. 2 Progressive release procedure and the use of a spring-like kinematic constraint to represent intermediate crack positions.

Consider a pure mode I loading, i.e., $G_{I_{max}} = G^i_{T_{max}}$. Assume that the energy release rate is such that the crack starts to grow, and designate that energy release rate $\widetilde{G}_I$ given by:

$$\widetilde{G}_I = \frac{F^i_{z_{max}} \delta^j_{z_{max}}}{2A^i} \tag{6}$$

For a linear elastic case, assuming self-similar conditions as the crack propagates, the force $F^i_{z_{max}}$ is assumed to linearly decrease:

$$F_z^i = F_{z_{max}}^i \left(1 - \frac{\Delta A}{A^i}\right) = F_{z_{max}}^i (1 - d) \tag{7}$$

where ΔA represents an intermediate crack position and $d \in [0,1]$ is defined as $d = \frac{\Delta A}{A^i}$, such that if $d = 1$ the node is completely released, and force F_z^i at the node pair i reduces to zero. Using the same assumptions, a similar relationship to Equation 7 can be written for the displacement jump:

$$\delta_z^i = \delta_{z_{max}}^j d \tag{8}$$

where δ_z^i is the displacement jump at node position i, which will equal $\delta_{z_{max}}^j$ when the node pair is completely released. Alternatively, the relationships given in (7) and (8) can be combined and written as:

$$F_z^i = m_z \delta_z^i + b_z \tag{9}$$

where $m_z = -\frac{F_{z_{max}}^i}{\delta_{z_{max}}^j}$ and $b_z = F_{z_{max}}^i$. For a given value d, Eq. (9) can also be written as:

$$F_z^i = k_z \delta_z^i = m_z \left(1 - \frac{1}{d}\right) \delta_z^i \tag{10}$$

and hence the stiffness of the spring k_z between node pair i^+ and i^- can be expressed as:

$$k_z = m_z \left(1 - \frac{1}{d}\right) \tag{12}$$

Equations (9) and (10) are represented graphically in Fig. 3~~Fig. 3~~ for a partially released case, i.e., $d \neq 0$.

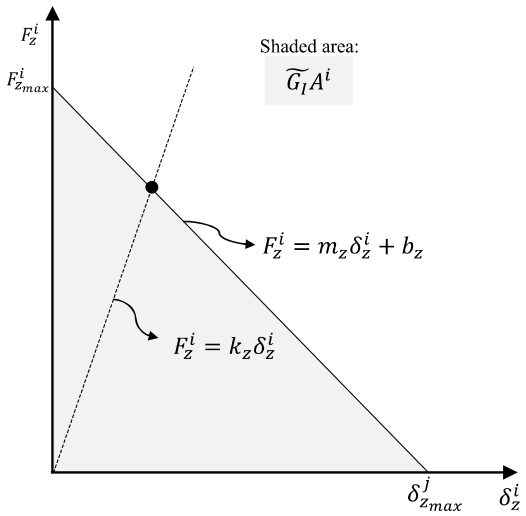

Fig. 3 Progressive release relationship between force and displacement jump, Eqs. (9) and (10).

Furthermore, Eq. (10) can be generally written for all degrees of freedom as:

$$\boldsymbol{f}_{VCCT}^i = \boldsymbol{M} \left(1 - \frac{1}{d}\right) \boldsymbol{\delta}^i \tag{13}$$

where:

$$\boldsymbol{M} = \begin{bmatrix} m_x & 0 & 0 \\ 0 & m_y & 0 \\ 0 & 0 & m_z \end{bmatrix} \tag{14}$$

Typically, delaminations grow under generic mixed-mode conditions. Assuming that the crack starts to grow past nodal position i with $\widetilde{G_I}$ and $\widetilde{G_{II}}$ calculated using VCCT:

$$\widetilde{G_I} = \frac{1}{2A^i} F^i_{z_{max}} \, \delta^j_{z_{max}}$$
$$\widetilde{G_{II}} = \frac{1}{2A^i} F^i_{x_{max}} \delta^j_{x_{max}} \tag{15}$$

Mode III is ignored for simplicity, but can be considered in a similar fashion. Assuming self-similar growth, the relationship between force and displacement jump as the crack grows past a given node pair, Eqs (9) and (10) can be written for both z and x directions and illustrated in Fig. 4~~Fig. 4~~a and 4b. Note that these relationships are different for z and x directions. Assume that conditions change during the progressive release, and the new $\widetilde{G_I}^{new}$, $\widetilde{G_{II}}^{new}$ are different from the initial $\widetilde{G_I}$, $\widetilde{G_{II}}$ that lead to a finite amount of growth. This can occur as the crack propagates in a non-self-similar fashion. Alternatively, it can also occur as a result of unloading after some initial release, and re-loading with different loading conditions. Despite the different loading conditions, if no growth occurs during unloading and re-loading according to the fracture criterion/growth law assumed, the spring stiffnesses, k_z^U and k_z^R should be identical and equal to k_z :

$$k_z^U = m_z^U \left(1 - \frac{1}{d^R}\right)$$
$$k_z^R = m_z^R \left(1 - \frac{1}{d^U}\right) \tag{16}$$

where the superscripts (U) and (R) designate variables associated with unloading (U) and re-loading (R).

$$k_z^U = k_z^R = k_z \tag{17}$$

In addition, since no growth occurs, also:

$$d^U = d^R = d \tag{18}$$

Recalling Eq. 12, Eqs. 17 and 18 are satisfied if:

$$m_z^U = m_z^R = m_z \tag{19}$$

and thus m_z is considered constant during the progressive release. Using similar arguments, m_x and m_y are also considered constant during the progressive release. This guarantees that no crack growth/healing occurs as a result of variation of loading conditions alone, without a fracture criterion or growth law being met. Using this condition, and Eqs (7), (8) and (10) in Eq. (15), G_I^p, G_{II}^p, and G_{III}^p are determinable for a partially released node:

$$G_I^p = -\frac{m_z \delta_z^i}{2d^2 A^i}$$
$$G_{II}^p = -\frac{m_x \delta_x^i}{2d^2 A^i} \tag{20}$$

$$G_{III}^{p} = -\frac{m_y \delta_y^i}{2d^2 A^i}$$

and re-assess fracture criterion or growth law. As a result, if the loading conditions change, the unloading curves described by Eq. 20 may shift, since $\widetilde{G_I} = G_I^p$ and $\widetilde{G_{II}} = G_{II}^p$ may vary, but the slopes remain constant as illustrated in Fig. 4~~Fig. 4~~(c) and (d).

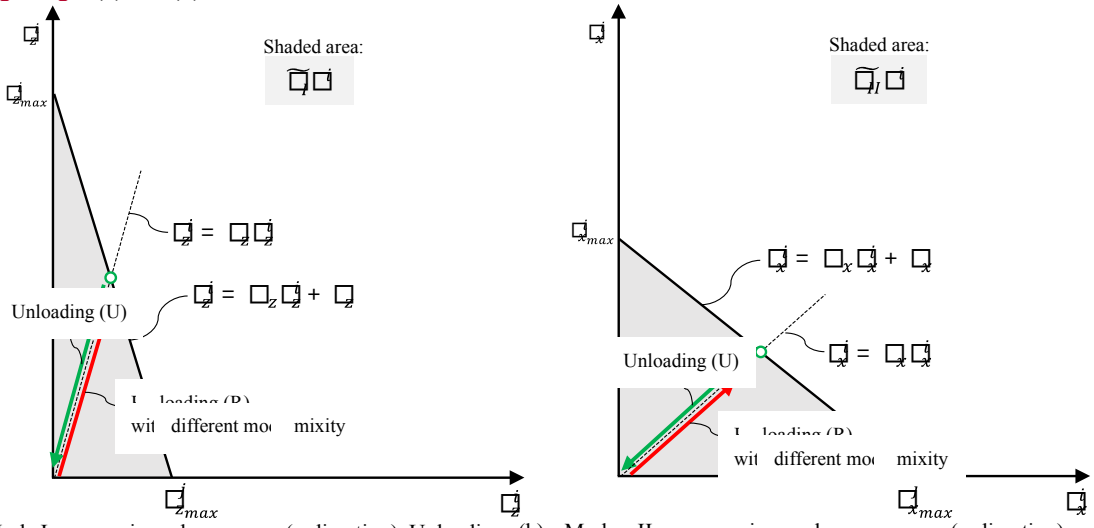

(a) Mode I progressive release curve (z-direction). Unloading and re-loading should follow the same slope.

(b) Mode II progressive release curve (x-direction). Unloading and re-loading should follow the same slope.

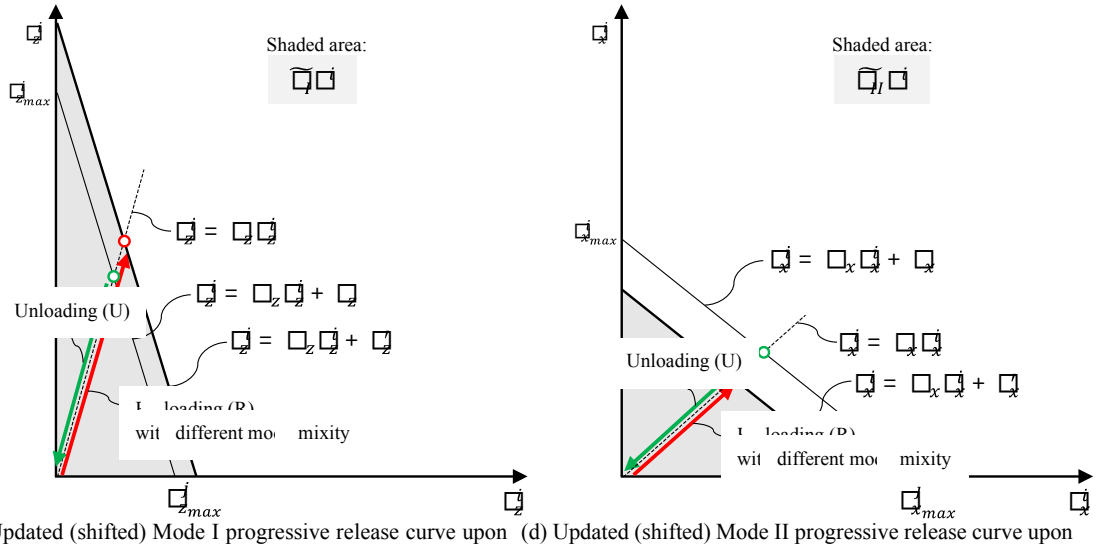

(c) Updated (shifted) Mode I progressive release curve upon re-loading as a result of a change in loading conditions, (z-direction).

(d) Updated (shifted) Mode II progressive release curve upon re-loading as a result of a change in loading conditions, (x-direction).

Fig. 4 Variation of the progressive release relationships as a consequence of a change in mode mixity due to unloading and re-loading with different loading conditions.

In the present implementation, an initial high-penalty stiffness, k_p, was assumed between node pairs that have not yet released. Considering the penalty stiffness does not affect the previous arguments, but leads to modified expressions for energy release rate and progressive release. These expressions are given below for mode I and direction z and are equivalent for other mode-mixities and loading directions:

$$F_S = \begin{cases} k_p\left({\delta'}_z^i + \delta_{z_0}^i\right), & {\delta'}_z^i \le 0 \\ m'_z\left(1 - \frac{1}{d}\right){\delta'}_z^i, & {\delta'}_z^i \ge 0 \end{cases} \tag{21}$$

in which:

$${\delta'}_z^i = {\delta}_z^i - \delta_{z_0}^i \tag{22}$$

where $\delta_{z_0}^i = \frac{F_{z_{max}}^i}{k_p}$, and:

$$m'_z = -\frac{F_{z_{max}}^i}{\delta_{z_{max}}^j - \delta_{z_0}^i} \tag{23}$$

and:

$$d = \frac{{\delta'}_z^i}{\delta_{z_{max}}^j - \delta_{z_0}^i} \tag{24}$$

Finally, the energy release rate for nodes that have started their partial release, and hence ${\delta'}_z^i > 0$, can be determined by:

$$G_I^p = -\frac{m'_z {\delta'}_z^i\left({\delta'}_z^i + \delta_{z_0}^i d\right)}{2d^2 A^i} \tag{25}$$

C. Fatigue crack growth law

In fatigue, crack growth is assumed to be well characterized by an exponential growth law, e.g., Paris Law, of the type:

$$\left(\frac{da}{dN}\right) = C\left(G_{T_{max}}\right)^n \tag{26}$$

where C and n are determined experimentally. Note that C and n can also be a function of other variables including mode mixity. For the nodes at the crack front that have not started to be released, Eq. (26) can be evaluated by replacing $G_{T_{max}}$ by the computed energy release rate using VCCT:

$$\left(\frac{da}{dN}\right)^i = C\left(G_{T_{max}}^i\right)^n \tag{27}$$

Having determined $\left(\frac{da}{dN}\right)^i$, it is possible to determine approximately how many cycles are needed to propagate the crack by a fraction $0 < \lambda \le 1$ of the element length, see Fig. 5a. Here. the element length a_l^i is determined along the node pair i, j correspondent to $G_{T_{max}}^i$, Fig. 1~~Fig. 1~~:

$$\Delta N_\lambda^i \approx \frac{\lambda a_l^i}{\left(\frac{da}{dN}\right)^i} \tag{28}$$

It is possible to determine the total number of cycles needed to propagate the crack to the next nodal position using:

$$\Delta N_{a_l}^i \approx \frac{a_l^i(1-d^i)}{\left(\frac{da}{dN}\right)^i} \tag{29}$$

where:

$$d^i = \frac{\Delta A}{A^i} = \frac{a_w^i a_{acc}^i}{a_w^i a_l^i} = \frac{a_{acc}^i}{a_l^i} \tag{30}$$

and a_{acc}^i represents the accumulated crack growth. Subsequently, for each node i at the crack front, ΔN^i is determined:

$$\Delta N^i = min\{\Delta N_\lambda^i, \Delta N_{a_l}^i\} \tag{31}$$

where ΔN^i is the minimum number of cycles needed to either propagate the crack by the set increment λa_l^i or to grow it to the next nodal position. Afterwards, the minimum of all ΔN^i determined for each node i along the crack front is computed:

$$\Delta N_{inc} = min\{\Delta N^1, \dots, \Delta N^i, \dots, \Delta N^m\} \tag{32}$$

In this increment, all nodes at the crack front are fatigued by ΔN_{inc} cycles. This assumption ensures that the set crack increment λa_l^i is not exceeded anywhere in the model, and that the crack does not accumulate beyond a_l^i such that at any time $d \leq 1$. Knowing ΔN_{inc}, the increment in Δd^i can be computed by:

$$\Delta d^i = \frac{\left(\frac{da}{dN}\right)^i \Delta N_{inc}}{a_l^i} \tag{33}$$

and the updated d_{new}^i can be computed as:

$$d_{new}^i = d^i + \Delta d^i \tag{34}$$

A node is considered to fail when:

$$d_{new}^i = 1 - \xi \tag{35}$$

The tolerance ξ provides a measure of the accumulation of crack growth required before a node is completely released, enabling the per-increment release of multiple nodes along the front (all the nodes meeting Eq. (35)), accelerating the analysis, see Fig. 5a.

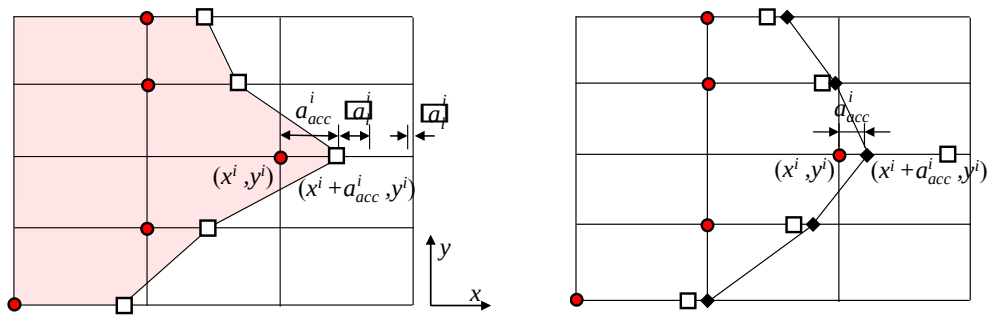

(a) Unsmoothed crack front

(b) Smoothed crack front

Fig. 5 Crack front (in-plane) definition and smoothing. Red circles represent nodes being released; squares intermediate crack positions; diamonds updated crack positions.

D. Equilibrium equations

Consider the equilibrium of a generic linear elastic solid subject to external forces, $\mathbf{f}_{\text{ext}}$, with internal stresses, $\boldsymbol{\sigma}$, in which partially released springs, $\mathbf{f}_{\text{VCCT}}(\boldsymbol{\delta})$, are included to represent intermediate crack positions:

$$\int_{\Omega} \boldsymbol{\sigma}\, d\Omega + \boldsymbol{f}_{VCCT}(\boldsymbol{\delta}) + \boldsymbol{f}_{ext} = 0 \tag{36}$$

Using the principal of virtual work, and recalling Eq. 13:

$$\mathrm{l}(\boldsymbol{u}) = \int_{\Omega} \boldsymbol{B}^t \boldsymbol{C} \boldsymbol{B} \boldsymbol{u}\, d\Omega + \underbrace{\boldsymbol{D}^t \boldsymbol{M} \left(1 - \frac{1}{d}\right) \boldsymbol{D} \boldsymbol{u}}_{\boldsymbol{f}_{VCCT}} + \boldsymbol{f}_{ext} = 0 \tag{37}$$

where $\boldsymbol{\varepsilon} = \mathbf{B}\mathbf{u}$, $\boldsymbol{\sigma} = \mathbf{C}\boldsymbol{\varepsilon}$, $\boldsymbol{\delta} = \mathbf{D}\mathbf{u}$.

Following the procedure outlined in the previous section, d is updated at the end of each converged increment leading to an explicit crack propagation. In this case, Eq. (37) is linear and solvable. The explicit crack propagation option leads to a linear system of equations with no convergence difficulties. However, it may require the use of a crack front smoothing strategy. Alternatively, letting d be determined within each increment results in an implicit crack propagation. The implicit crack propagation may alleviate the requirement for a crack front smoothing algorithm. However, since d will also be a function of $\mathbf{u}$, this leads to a nonlinear system of equations and convergence challenges. A comparison between these two algorithms is out of the scope of the present work.

E. Crack front smoothing

In the present approach, the virtual crack front can be found by adding the value of the accumulated crack growth, a^i_{acc}, to the nodal coordinates, see Fig. 5~~Fig. 5~~. Under certain conditions, small perturbations in energy release rate may lead to local crack distortion that amplifies as the crack grows, ultimately leading to an incorrect crack front shape. Mesh refinement, the use of small release tolerances, and crack increments may attenuate this effect at the expense of an increase in computational time. In the present work, a smoothing step is implemented to address this issue. Several techniques can be used, such as a polynomial fit to the crack front [16]. In the proposed approach, Gaussian averaging [17] is performed such that each crack position x^i is averaged based on a Gaussian distribution where σ_{gauss} is the standard deviation of the assumed Gaussian curve. The nodes used to obtain an average position for x^i are selected within a $[-3\sigma_{gauss}, 3\sigma_{gauss}]$ distance interval centered in x^i. After smoothing, a^i_{acc} is recomputed (Fig. 5b), and d is determined, see previous section. To facilitate the implementation and assessment of the algorithm, only the coordinate x along the specimen length is smoothed.

F. Implementation

The method is implemented via an 8 noded user element. The element is placed between 3D native Abaqus elements along the delamination plane, and is used to model delamination growth by changing the value of the stiffness prescribed between node pairs as outlined in the previous section. The present algorithm assumes that the growth rate is written in the form shown in Eq. (26). Other forms for the growth rate as a function of energy

release rate may require modifications to the algorithm, including additional finite element analysis. As mentioned previously, the present algorithm is event-based, where an event is defined as a growth increment and or a node being completely released. Although event-based algorithm was chosen for illustrative purposes, other algorithms, such as cycle-based, could also be explored using the same overall methodology.

The solution is obtained as follows:

- Step (1) An implicit finite element analysis is performed, and nodal forces and displacements are obtained for all nodes at the crack front Eq. (37). The energy release rates are determined using Eq. (5) for nodes at the crack front that have not started to release yet or Eq. (20) for nodes that have been partially released.
- Step (2) Knowing the energy release rate at each node, the growth rate can be determined, Eq. (27)
- Step (3) The cycle increment, ΔN_{inc}, is computed, Eq. (32)
- Step (4) The incremental crack growth for each node i at the front, Δd^i is computed using Eq. (33) and accumulated via Eq. (34), obtaining an updated d^i_{new}. As an option, smoothing can be performed between Step 4 and Step 5, resulting in an adjusted accumulated crack growth.
- Step (5) d^i_{new} is set to 1 for all nodes at the crack front for which Eq. (35) is satisfied.
- Step (6) The total cycle count is updated, $N_{Total} = N_{Total} + \Delta N_{inc}$, and the procedure is repeated.

III. Results

Models of the Double Cantilever Beam (DCB), Mixed Mode Bending (MMB), and End Notch Flexure (ENF) tests were developed and shown in Fig. 6. These models were used to verify the approach proposed, for mode mixities ranging from pure Mode I to pure Mode II. Dimensions, mesh refinement, boundary conditions, and material properties were based on those used in the benchmark solutions in [18-20], so that the accuracy of this approach could be compared to the benchmarks. The material properties are summarized in Tables I to IV. The present section provides an assessment of the sensitivity of the energy release rate calculation, its mesh independency, and overall crack shape development towards the various solution parameters. Subsequently, the accuracy of the approach was evaluated by comparing the results obtained for crack growth as a function of number of cycles to the benchmark results given in [18–20] for the DCB, MMB and ENF cases.

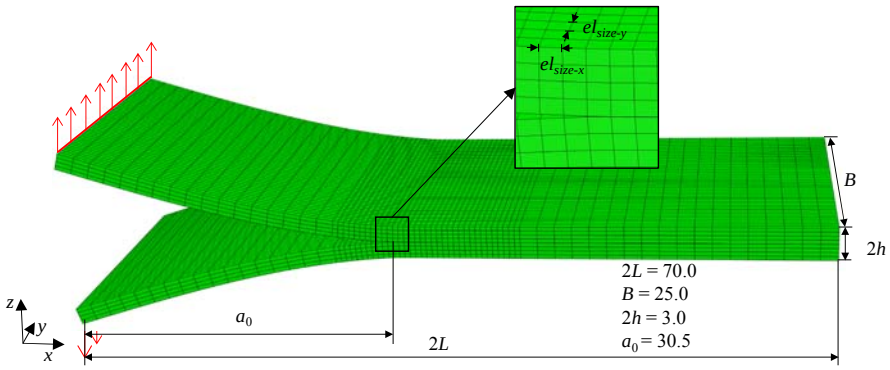

(a) DCB

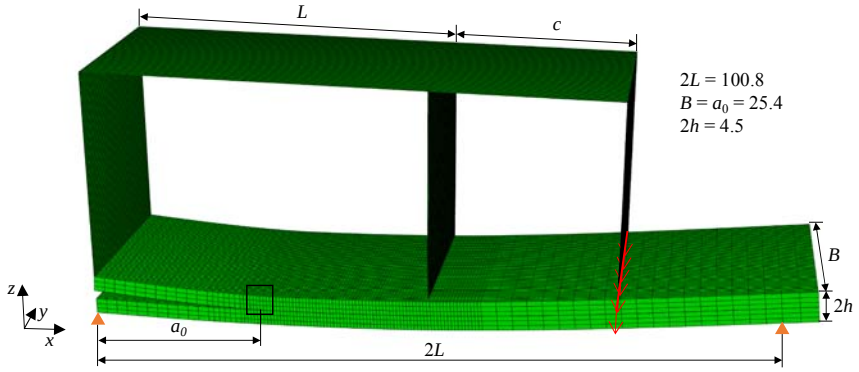

(b) MMB

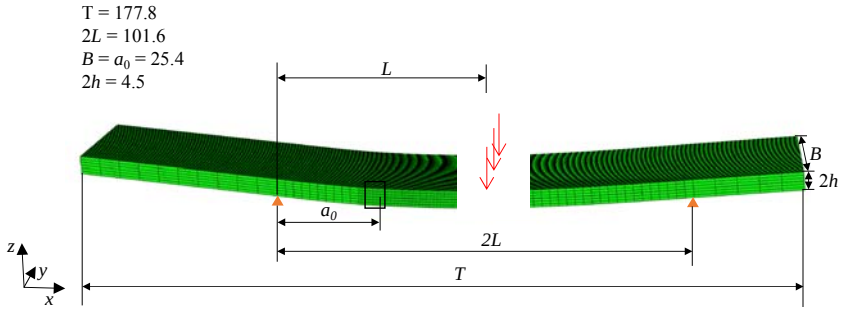

(c) ENF

Fig. 6 DCB, MMB and ENF models. Dimensions, mesh and boundary conditions based on [18–20]. All dimensions shown are in mm.

TABLE I ELASTIC PROPERTIES, AND PARIS LAW COEFFICIENT $\boldsymbol{C}$ AND EXPONENT $\boldsymbol{n}$ USED IN THE DCB BENCHMARK [18].

E_{11} [GPa]	$E_{22} = E_{33}$ [GPa]	$G_{12} = G_{13}$ [GPa]	G_{23} [GPa]	$\nu_{12} = \nu_{13}$ [−]	ν_{23} [−]	C $\left[\frac{\text{mm}}{\text{cycle}}\left(\frac{\text{kJ}}{\text{m}^2}\right)^{-n}\right]$	n [−]
139.4	10.16	4.6	3.99	0.3	0.44	2.44×10^6	10.61

TABLE II ELASTIC PROPERTIES, USED IN THE MMB AND ENF BENCHMARKS [19, 20].

E_{11} [GPa]	$E_{22} = E_{33}$ [GPa]	$G_{12} = G_{13}$ [GPa]	G_{23} [GPa]	$\nu_{12} = \nu_{13}$ [−]	ν_{23} [−]
161	10.38	5.17	3.98	0.32	0.44

TABLE III PARIS LAW COEFFICIENT $\boldsymbol{C}$ $\left[\frac{\text{mm}}{\text{cycle}}\left(\frac{\text{kJ}}{\text{m}^2}\right)^{-n}\right]$ USED IN THE MMB AND ENF BENCHMARKS AS A FUNCTION OF MODE-MIXITY $\boldsymbol{\beta = G_{II}/G_T}$ [19, 20].

$\beta = 0.2$	$\beta = 0.5$	$\beta = 0.8$	$\beta = 1.0$
2412	6.79	4.58	0.33

TABLE IV PARIS LAW EXPONENT $\boldsymbol{n}$ USED IN THE MMB AND ENF BENCHMARKS AS A FUNCTION OF MODE MIXITY [19, 20].

$\beta = 0.2$	$\beta = 0.5$	$\beta = 0.8$	$\beta = 1.0$
8.4	5.4	4.1	5.55

A. Crack shape

Fig. 7~~Fig. 7~~ shows the planar view of the crack front obtained in a DCB model after a few increments of growth. The thumbnail shape obtained was characteristic of DCB specimens [15]. Note that the crack was initially straight, as highlighted in Fig. 7~~Fig. 7~~. The gridlines correspond to element boundaries. It is evident from Fig. 7~~Fig. 7~~ that the procedure proposed was capable of accommodating a crack front which does not conform to the underlying mesh, developing in a mesh-independent fashion. Indeed, the crack was seen to traverse multiple element boundaries without any visible effect on its smoothness or shape.

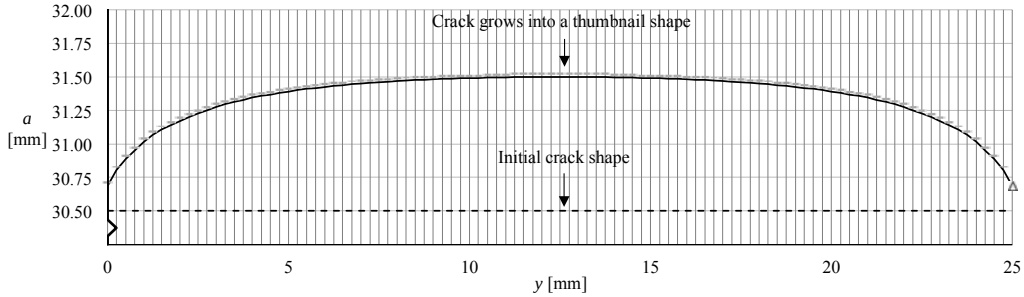

Fig. 7 Planar view of the crack front traversing multiple elements (gridlines). The vertical axis is expanded to facilitate the visualization of the crack front shape.

B. Sensitivity Study

In the present section, the energy release rate calculation and the simulated crack shape were assessed as a function of mesh size, crack growth increment λ, release tolerance ξ, and smoothing. In Fig. 8, the crack front shape and energy release rate along the crack front of a DCB specimen are illustrated. Both energy release rate distribution and crack front shape were obtained for the increment correspondent to a maximum crack length of $\max(a_T) = 35.5$ mm. Progressively finer meshes, with element sizes correspondent to $el_{size-x} = el_{size-y} = \{1.0, 0.5, 0.25\}$ mm, were used, see Fig. 6a. All meshes used captured the typical thumbnail shape observed in DCB specimens. However, progressively finer meshes generally led to a smoother crack front, and more pronounced thumbnail shapes, (Fig. 8a), with a smoother energy release rate along the crack front, (Fig. 8b). In Fig. 9, the effect of the crack increment λ on both crack shape and energy release rate along the crack front was

assessed by varying λ, while keeping mesh refinement and release tolerance ξ constant. It was apparent from Fig. 9 that decreasing the crack increment λ leaded to a slightly smoother crack shape (Fig. 9a), and energy release rate distribution along the width, (Fig. 9b). Note that a broad range of crack increments were used, from $\lambda = 0.125$ (requiring 430 increments) to a maximum $\lambda = 1.0$ (requiring 370 increments to propagate a crack 10 mm), without significantly compromising the solution. . Therefore, after a small number of growth increments, the overall crack advancement becomes dominated by the release tolerance requirement of Eq. 35. In Fig. 10, a similar assessment was performed regarding the release tolerance ξ. A release tolerance of $\xi = 0.1$ seems to compromise the smoothness of the crack front obtained, (Fig. 10a), and the energy release rate distribution, Fig. 10b. Decreasing ξ leads to progressively smoother crack front shapes and energy release rate distributions at the expense of additional crack increments; while $\xi = 0.1$ required 150 increments, $\xi = 0.02$ required 350 increments for 10 mm of crack propagation.

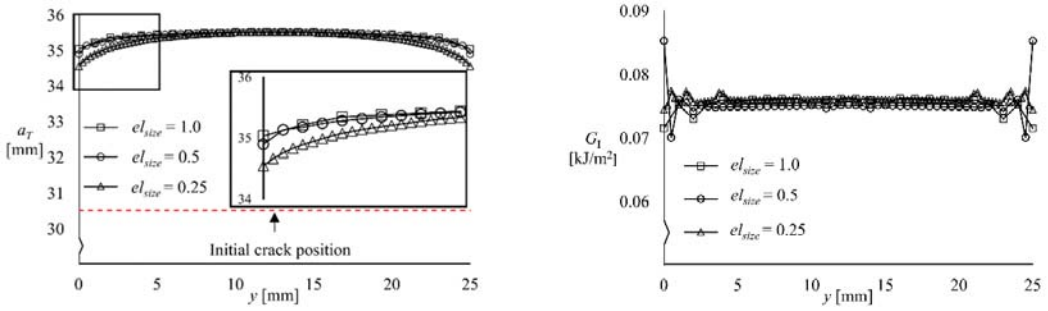

(a) crack front shape (b) energy release rate

Fig. 8 Effect of mesh refinement on crack front shape and energy release rate distribution along the crack front, for a crack in a DCB specimen that propagated from $a_T = a_0 = 30.5$ mm to max$(a_T) = 35.5$ mm. Results obtained with $\lambda = 0.25$, $\xi = 0.01$ and $el_{size-x} = el_{size-y} = el_{size}$ mm.

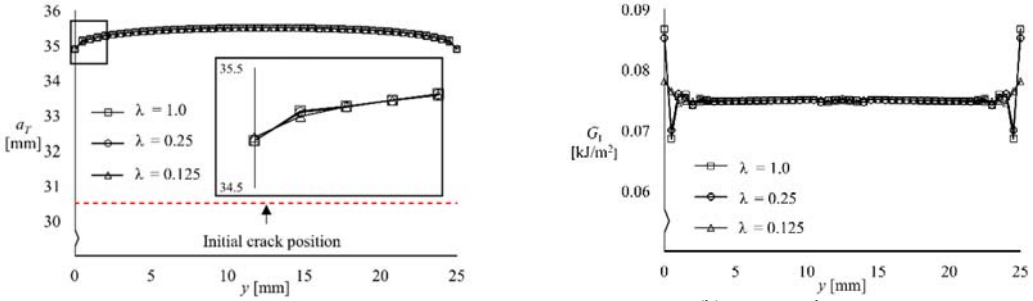

(a) crack front shape (b) energy release rate

Fig. 9 Effect of growth increment on crack front shape and energy release rate distribution along the crack front, for a crack in a DCB specimen that propagated from $a_T = a_0 = 30.5$ mm to max$(a_T) = 35.5$ mm. Results obtained with $\xi = 0.01$ and $el_{size-x} = el_{size-y} = el_{size} = 0.25$.

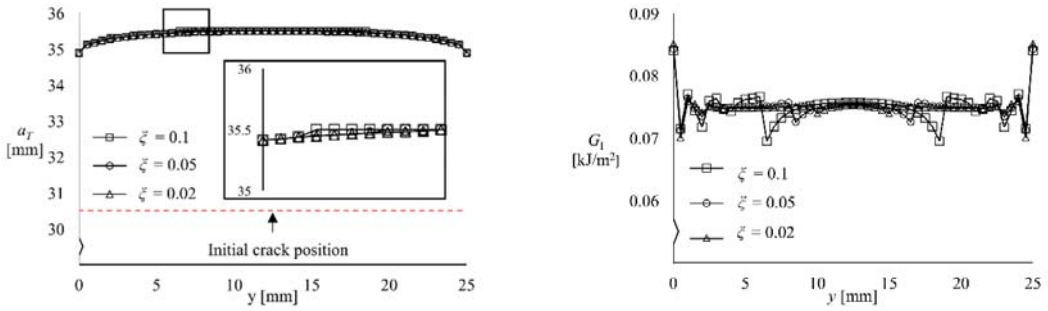

(a) crack front shape (b) energy release rate

Fig. 10 Effect of release tolerance on crack front shape and energy release rate distribution along the crack front, for a crack in a DCB specimen that propagated from $a_T = a_0 = 30.5$ mm to $\max(a_T) = 35.5$ mm. Results obtained with $\lambda = 0.25$ and $el_{size-x} = el_{size-y} = el_{size} = 0.25$.

For the DCB case, Gaussian smoothing was not required to obtain a smooth crack front shape, Figs. 8 to 10. For the MMB and ENF cases, depending on the mesh size used and the element aspect ratio (in-plane), small perturbations of the crack front shape could interact and diverge, leading to a crack front with a non-realistic zigzag shape. This is illustrated in Fig. 11~~Fig. 11~~ where jagged crack front shapes, obtained at two different increments in an MMB specimen, with mode-mixity $\beta = \frac{G_{II}}{G_T} = 0.8$ are plotted. This behavior was attenuated with an increase in mesh refinement, as can be seen by comparing the crack front shape obtained with el_{size} = 0.25 mm and el_{size} = 0.125 mm in Fig. 11~~Fig. 11~~. Alternatively, the crack front labeled 'Smoothed' in Fig. 11~~Fig. 11~~ indicates that a small degree of Gaussian smoothing was sufficient to eliminate the jagged crack front, even for the coarser mesh el_{size} = 0.25 mm, while capturing the overall crack front shape.

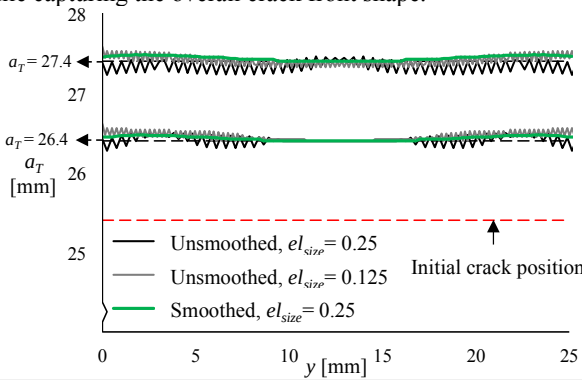

Fig. 11 Effect of smoothing the crack front of an 80% Mode II MMB model. Results obtained with element size $el_{size} = \{0.125, 0.25\}$ mm, crack growth increment $\lambda = 0.25$ and release tolerance $\xi = 0.01$.

C. Verification

In this section, results obtained from DCB (Mode I), MMB (Mixed Mode I/II) and ENF (Mode II) models are presented and compared to 2D benchmark results [18–20]. For all cases, the solution parameters were kept constant, including: mesh size $el_{size-x} = 0.5$ mm, $el_{size-y} = 0.25$ mm; the crack growth increment ratio $\lambda = 0.25$; the release tolerance $\xi = 0.01$; and smoothing $\sigma_{gauss} = el_{size-y}$. All cases approximate well the benchmark solution, as shown in Fig. 12. The figures also include a representative steady state crack shape for each of the models, as determined by the simulations. Small discrepancies observed were attributed to the 3D models used in this study versus the assumed plane strain conditions and straight crack front of the benchmarks.

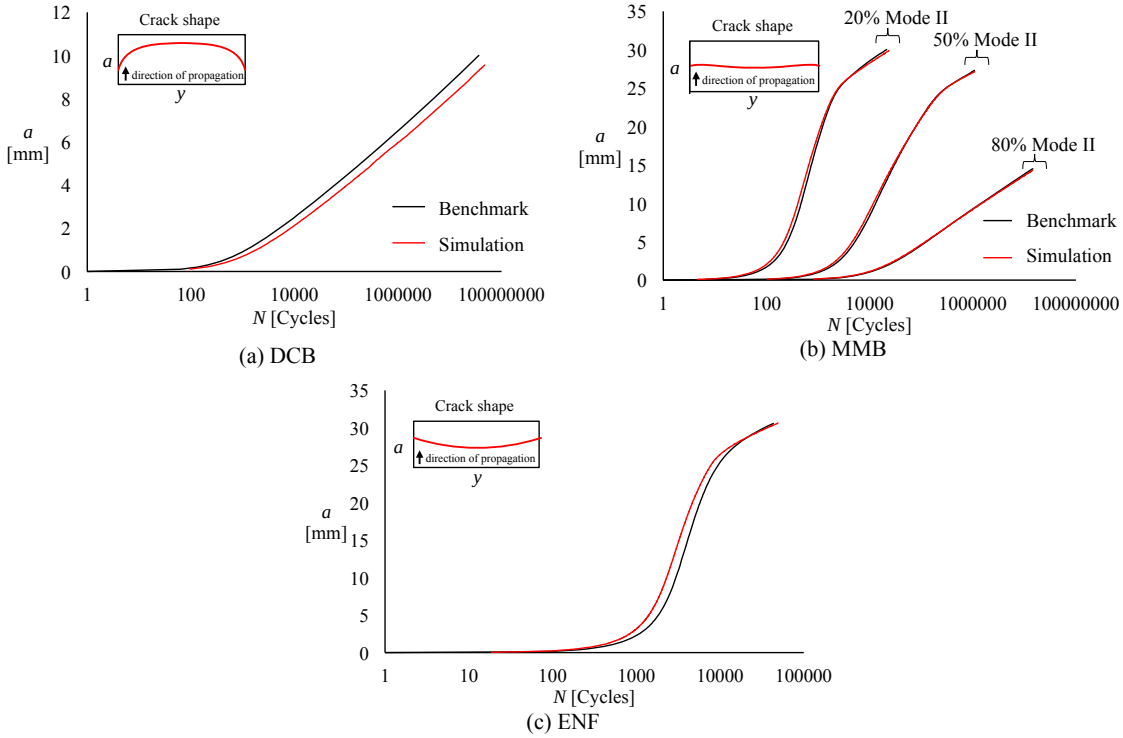

Figure 12 DCB, MMB and ENF results and comparison with 2D fatigue benchmarks.

Overall, the results presented demonstrate that the approach proposed was successfully used to model the fatigue growth of crack shapes that do not conform to the underlying mesh. Mesh refinement, maximum crack growth increment λ, and release tolerance ξ all affect the solution. However, they show a convergent behavior, i.e., decreasing these parameters leads to smoother crack shapes and energy release rate distributions along the crack front. The smoothing procedure was shown to be particularly useful in the ENF specimen and demonstrated the ability to efficiently address the zigzag crack front observed in those specimens without requiring additional mesh refinement.

IV. Summary

A novel approach was proposed that combines progressive nodal release with VCCT to model fatigue crack growth in a mesh-independent fashion. By performing the progressive nodal release, crack shapes that do not conform to the underlying mesh could be readily modeled. Sensitivity studies demonstrated that the method proposed enables the accurate calculation of intermediate energy release rates, and shows an overall convergent behavior. The approach was demonstrated using DCB, MMB and ENF models, which produced accurate results compared to benchmark solutions for mode mixities ranging from $0 \leq \beta \leq 1$. As proposed, this approach can be used with any functional form of energy release rate to characterize delamination growth rate. Additionally, since growth is determined as a post-processing step at the end of each increment, it shows no convergence issues associated with the progressive nodal release.

Acknowledgements

The material is based upon work supported by NASA under Award No. NNL09AA00A. Any opinions, findings, and conclusions or recommendations expressed in this material are those of the author(s) and do not necessarily reflect the views of the National Aeronautics and Space Administration.

References

[1] E.F. Rybicki, M.F. Kanninen. A finite element calculation of stress intensity factors by a modified crack closure integral. *Engineering Fracture Mechanics*, 9(4):931–938, 1977.

[2] I.S. Raju, R. Sistla, and T. Krishnamurthy. Fracture mechanics analyses for skin-stiffener debonding. *Eng. Fract. Mech.* 54(3):371–385, 1996.

[3] E.H. Glaessgen, I.S. Raju, and C.C. Poe. Fracture mechanics analysis of stitched stiffener-skin debonding. The 39th AIAA/ASME/ASCE/AHS/ASC Structures, Structural Dynamics and Materials Conference, Long Beach, California, AIAA 98-2022, April 20–23, 1998.

[4] R. Krueger. Virtual crack closure technique: history, approach, and applications. *Applied Mechanics Reviews*, 57(2):109 – 143, 2004.
[5] M.F.S.F. De Moura, J.P.M. Gonçalves, A.T. Marques, and P.M.S. Tavares De Castro. Modeling compression failure after low velocity impact on laminated composites using interface elements. *Journal of Composite Materials*, 31(15):1462 – 1479, 1997.
[6] P.P. Camanho and C.G. Dávila. Mixed-mode decohesion finite elements for the simulation of delamination in composite materials. Technical report, NASA-TM-2002-211737, National Aeronautics and Space Administration, 2002.
[7] S. Rinderknecht and B. Kröplin. A computational method for the analysis of delamination growth in composite plates. *Computers & Structures*, 64(1):359 – 374, 1997.
[8] B.R. Davis, P.A. Wawrzynek, and A.R. Ingraffea. 3-D simulation of arbitrary crack growth using an energy-based formulation - part I: Planar growth. *Engineering Fracture Mechanics*, 115:204 – 220, 2014.
[9] De Xie and S.B. Biggers Jr. Strain energy release rate calculation for a moving delamination front of arbitrary shape based on the virtual crack closure technique. part I: Formulation and validation. *Engineering Fracture Mechanics*, 73(6):771 – 785, 2006.
[10] A. C. Orifici, R. S. Thomson, R. Degenhardt, C. Bisagni, and J. Bayandor. Development of a finite-element analysis methodology for the propagation of delaminations in composite structures. *Mechanics of Composite Materials*, 43(1):9– 28, 2007.
[11] E. Pietropaoli and A. Riccio. On the robustness of finite element procedures based on virtual crack closure technique and fail release approach for delamination growth phenomena. Definition and assessment of a novel methodology. *Composites Science and Technology*, 70(8):1288 – 1300, 2010.
[12] G.E. Mabson, L.R. Deobald, B. Dopker, D.M. Hoyt, J.S. Baylor, D.L. Graesser. Fracture interface elements for static and fatigue analysis. In: 16th International conference on composite materials, Kyoto, July 2007.
[13] L. Deobald, G. Mabson, B. Dopker, and D. Graesser. Interlaminar fatigue elements for crack growth based on virtual crack closure technique. In Proceedings of the 48th AIAA/ASME/ASCE/AHS/ASC Structures, Structural Dynamics and Materials Conference, 2007.
[14] Abaqus Analysis User's Manual, Abaqus/Standard DSS Simulia, 6.17 edition, 2017.
[15] B.D. Davidson. An analytical investigation of delamination front curvature in double cantilever beam specimens. *Journal of Composite Materials*, 24(11):1124–1137, 1990.
[16] P.A. Wawrzynek, B.J. Carter, and A.R. Ingraffea. Advances in simulation of arbitrary 3D crack growth using FRANC3D NG. In Proceedings of the 12th International Conference on Fracture, Ottawa, Ontario, Canada, 2009.
[17] R.M. Haralock and L.G. Shapiro. Computer and robot vision. Addison-Wesley Longman Publishing Co., Inc., 1991.
[18] R. Krueger. Development of a benchmark example for delamination fatigue growth prediction. Technical Report NASA/CR-2010-216723, National Aeronautics and Space Administration, 2010.
[19] R. Krueger. Development and application of benchmark examples for mode II static delamination propagation and fatigue growth predictions. Technical Report NASA/CR-2011-217305, National Aeronautics and Space Administration, 2011.
[20] R. Krueger and N.V. De Carvalho. In search of a time efficient approach to crack and delamination growth predictions in composites. In Proceedings of the American Society for Composites 31st Technical Conference, Williamsburg, VA, USA, 2016.